Check for updates

The role of excited-state character, structural relaxation, and symmetry breaking in enabling delayed fluorescence activity in push–pull chromophores†

Patrick Kimber, [ID] Pooja Goddard, [ID] Iain A. Wright [ID] and Felix Plasser [ID] *

Thermally activated delayed fluorescence (TADF) is a current promising route for generating highly efficient light-emitting devices. However, the design process of new chromophores is hampered by the complicated underlying photophysics. In this work, four closely related donor–π–acceptor–π–donor systems are investigated, two of which were synthesised previously, with the aim of elucidating their varying effectiveness for TADF. We outline that the frontier orbitals are insufficient for discriminating between the molecules. Subsequently, a detailed analysis of the excited states at a correlated *ab initio* level highlights the presence of a number of closely spaced singlet and triplet states of varying character. Results from five density functionals are compared against this reference revealing dramatic changes in, both, excited state energies and wavefunctions following variations in the amount of Hartree–Fock exchange included. Excited-state minima are optimised in solution showing the crucial role of structural variations and symmetry breaking for producing a strongly emissive S_1 state. The adiabatic singlet–triplet gaps thus obtained depend strongly on the range separation parameter used in the hybrid density functional calculations. More generally, this work highlights intricate differences present between singlet and triplet excited state wavefunctions and the challenges in describing them accurately.

1 Introduction

Thermally activated delayed fluorescence (TADF) constitutes a promising route toward creating organic electroluminescent materials with the potential to obtain 100% internal quantum efficiency through the possibility of harvesting both singlet and triplet excitons.[1–3] On a microscopic level, TADF is governed by the reverse intersystem crossing (rISC) process whereby a non-emissive molecular triplet excited state is converted into an emissive singlet state capable of efficient luminescence. Most prominently, the rISC process depends on the energy gap (ΔE_{ST}) between the lowest excited singlet and triplet states, which enters exponentially into the rate expression[1] and can be seen as an effective activation energy to the TADF process. Other influences are related to spin–orbit coupling (SOC), enabling the formally spin-forbidden rISC process,[1] and the oscillator strength (f) of the emitting singlet state.[4] All three properties crucially depend on the state character where

enhanced charge transfer (CT) is expected to lower both ΔE_{ST} and f.[5] SOC, on the other hand, is promoted by a difference in state character between the singlet and triplet states[1,6,7] where small amounts of mixed character can already lead to appreciable coupling.[8] Furthermore, the importance of a second, locally excited (LE), triplet state has been emphasised.[6,9,10] Finally, multipolar systems are of interest where one acceptor unit is connected to two or more donor units and *vice versa*.[4,11] Aside from the above considerations, the possibility of symmetry breaking in the excited state is particularly intriguing in such multipolar systems.[11,12]

The intricate photophysics of TADF emitters poses severe challenges for its computational description while also providing an ideal test bed for evaluating the newest computational tools. The importance of CT states already makes it clear that the application of time-dependent density functional theory (TDDFT) is challenging in terms of describing energies[13] as well as state characters.[14] Suggestions for addressing this problem range from empirical corrections[15] to optimal tuning of range-separated functionals[7,16] to the avoidance of TDDFT altogether in favour of unrestricted ground-state DFT.[8,17] Furthermore, state-specific excited-state solvation effects have to be described at a high level considering that the common linear-response polarizable continuum model (LR-PCM) is inadequate for CT

Department of Chemistry, Loughborough University, Loughborough, LE11 3TU, UK.
E-mail: f.plasser@lboro.ac.uk; Tel: +44-1509-226946

† Electronic supplementary information (ESI) available: Relative energies of conformers, fragment definitions, range separation parameter tuning data, analysis of vertical excitations, and results for excited state geometries with larger range separation parameter. See DOI: 10.1039/d1cp03792g

This journal is © the Owner Societies 2021

Phys. Chem. Chem. Phys., 2021, **23**, 26135–26150 | 26135

states with large electron–hole separation[18,19] and does not even provide any correction beyond zeroth order to triplet states due to their vanishing transition densities. Finally, the importance of dynamic mixing effects,[20] structural deformations,[10] and vibronic coupling between the LE and CT triplet states[9,21] has been emphasised.

A common theme in the above discussions of TADF photophysics and its computational description is the importance of excited states of different character, in particular LE and CT states. Accurately analysing these states and the mixing between them can become a challenge on its own and a simple discussion of frontier orbitals is often inadequate. Thus, aside from the necessity of choosing an accurate electronic structure method, it becomes exceedingly important to choose a meaningful and reproducible method for analysing the computations. Indeed, a range of tools for categorising excited states are available. Categorisation of excited states occurs prominently *via* different measures of charge transfer,[22–25] which are a natural choice for push–pull systems. However, special care has to be taken for symmetric systems, including the molecules studied here, noting that the dipole moment and related charge displacement metrics are not reliable descriptors for the charge transfer character in symmetric systems.[24,26,27] A powerful option to overcome this problem amounts to base the analysis on a correlated electron–hole pair within an effective exciton picture;[28] and this was shown to be particularly suitable even for challenging cases with high symmetry.[29–31] Aside from categorising excited states, there has been an increasing push toward a rationalisation of the underlying energetics and, in particular, the singlet–triplet gap. The applied approaches range from a formal discussion of the underlying molecular orbital integrals[1,7] to a direct extraction of computational data from actual electronic structure computations and applying it for energy decomposition and visualisation.[5,32,33]

It is the purpose of this work to exemplify the above discussion on four different TADF candidates highlighting their intricate photophysics as well as methodological challenges in the computational description. The four molecules studied are shown in Fig. 1, all possessing a D–π–A–π–D structure where a central accepting moiety (A) is symmetrically connected to two donors (D) whose separation is controlled by 1,4-phenylene π-bridges. All molecules employ a carbazole (**Cz**) donor group and we use four different core groups, benzo[1,2-*b*:4,5-*b'*]dithiophene-4,8-dione (**BDT**), anthraquinone (**AQ**), benzo[1,2-*b*:4,5-*b'*]dithiophene-*S*,*S*-dioxide-4,8-dione (**BDT-SO₂**), and benzo[1,2-*b*:4,5-*b'*]difuran-4,8-dione (**BDF**). Two of these molecules **Cz-BDT**[34] and **Cz-AQ**[4] have been previously synthesised and characterised. We will study these in detail before moving on to predicting the properties of **Cz-BDT-SO₂** and **Cz-BDF**. Within this work, we contrast these four related molecules highlighting the profound changes in their observed photophysical properties following seemingly inconspicuous changes in the acceptor unit.

The employed acceptor unit **BDT** is an electron deficient ring-fused heterocycle and a synthetic intermediate towards the synthesis of the fully aromatic and strongly-electron donating benzodithiophene moiety which is widely exploited in high
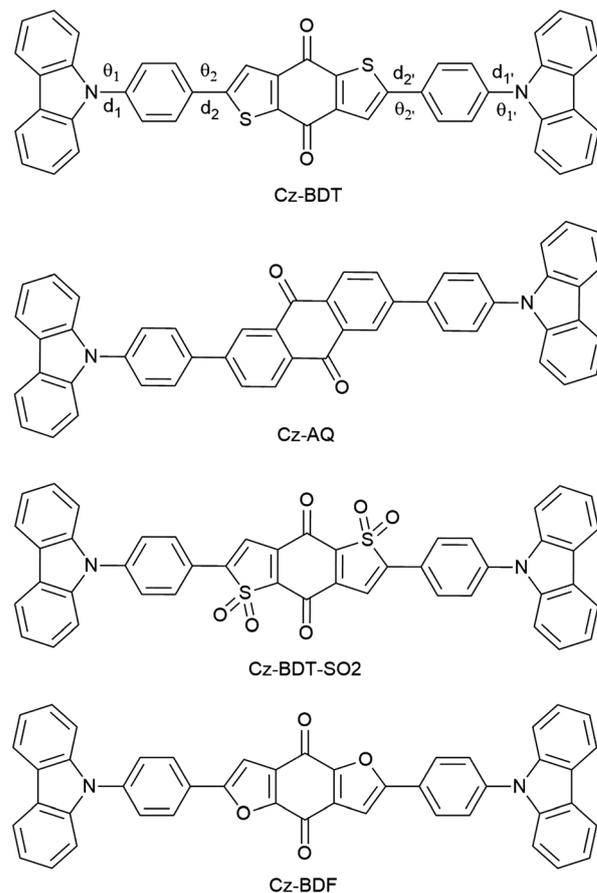

Fig. 1 The molecular structures of the four D–π–A–π–D molecules studied within this work. The dihedral angles and bond distances discussed throughout are indicated by θ_n and d_n, and are defined in the same way for all molecules in this work.

performance donor polymers for organic solar cells.[35–41] While benzodithiophene has seen great utilisation as a donor, **BDT** itself has received much less attention as an acceptor unit despite its deep LUMO energy which is *ca.* 0.39 V lower than that of the carbocyclic homologue anthraquinone.[42,43]

Cz-BDT was designed to complement one of the best reported red TADF luminogens at the time, **Cz-AQ**,[4] and induce a red-shift in emission due to the lower LUMO of **BDT**. This did lead to a >100 nm redshift in emission wavelength compared to **Cz-AQ**, and TADF was evident from the characteristic double decay in the transient absorbance spectra, however the photoluminescence quantum yield (PLQY) was greatly reduced in both solution and dilute thin film measurements from ≈0.60 for **Cz-AQ** in solution to <0.10 for **Cz-BDT**. We note that in the meantime alternative strategies in the design of red TADF emitters have led to high PLQY extending into the near infrared range.[44–51] Nonetheless, identifying the root cause of the vast drop in PLQY between **Cz-AQ** and **Cz-BDT** presents a useful challenge to inform future molecular design and to provide insight into the intricate photophysics of TADF emitters.

Here, we also study **Cz-BDT-SO₂** where dearomatisation of the fused heterocycles will serve to further reduce the LUMO

26136 | *Phys. Chem. Chem. Phys.*, 2021, **23**, 26135–26150

This journal is © the Owner Societies 2021

PCCP

Paper

(and to a lesser extent the HOMO) through inductive effects and remove the influence of the S lone pairs on the electronic properties of the molecule. Oxidation of S to SO_2 serves to stabilise the LUMO and red-shift emission while it is also expected to enhance PLQYs and modulate singlet and triplet energies, ΔE_{ST}, spin–orbit coupling effects, and solvatochromism.[52–55] Finally, **Cz-BDF** is studied in order to identify the impact of light vs. heavy heteroatoms on molecular geometries, excited state energies, and characters.

Within this work, we first explain the methods used discussing the general strategy employed for analysing excited-state wavefunctions and proceeding to specifics of the computational details. The results are presented in some detail starting with general structural parameters and frontier orbitals, proceeding to a discussion of the vertical excitations in terms of the state characters present and the computational description, finishing with an exploration of excited-state minima in solution. Before concluding, we proceed by a compact discussion summarising the main photophysical properties computed using two values of the hybrid DFT range separation parameter, highlighting general differences between singlet and triplet state wavefunctions, and reviewing the most critical methodological aspects.

2 Methods

2.1 Wavefunction analysis

Analysis of excited state wavefunctions is performed via TheoDORE,[56] which provides automatic, fragment-based assignment of state character. Specifically, the analysis uses the one-electron transition density matrix (1TDM), which is formally defined as:

$$\gamma_{0I}(r_h, r_e) = n \int \cdots \int \Psi_0(r_h, r_2, \ldots, r_n) \Psi_I(r_e, r_2, \ldots, r_n) dr_2, \ldots, dr_n \tag{1}$$

where Ψ_0 and Ψ_I are the ground and excited state wavefunctions and r_h and r_e represent the coordinates of the excitation hole and the excited electron respectively.[57] The excited state described by the 1TDM can be decomposed into local and CT contributions by computing the charge transfer numbers defined as the integral:[57,58]

$$\Omega_{AB} = \int_A \int_B |\gamma_{0I}(r_h, r_e)|^2 dr_e dr_h \tag{2}$$

where the hole and electron are restricted to fragment A and B respectively. Practically, eqn (2) is evaluated using a Mulliken-style population analysis,[57] here.

Excited states can also be analysed via the natural transition orbitals (NTOs),[22,59] computed through a singular value decomposition where the 1TDM is expressed as[57,58]

$$\gamma_{0I}(r_h, r_e) = \sum_t \sqrt{\lambda_t} \psi_t^h(r_h) \psi_t^e(r_e) \tag{3}$$

Eqn (3) describes a sum over orbital pairs where ψ_t^h and ψ_t^e are the NTOs representing the hole and electron, and λ_t is the amplitude of the transition. In the specific case that a state can be described by a single transition between two NTOs, in other words, the state is not multiconfigurational, the 1TDM can be factorised into a single pair of NTOs:

$$\gamma_{0I}(r_h, r_e) = \psi^h(r_h) \psi^e(r_e) \tag{4}$$

and the charge transfer numbers (eqn (2)) are:

$$\begin{aligned} \Omega_{AB} &= \int_A \int_B |\psi^h(r_h) \psi^e(r_e)|^2 dr_e dr_h \\ &= \int_A |\psi^h(r_h)|^2 \times \int_B |\psi^e(r_e)|^2 dr_e = q_A^h q_B^e. \end{aligned} \tag{5}$$

Thus, for simple transitions involving only one orbital pair, the charge transfer numbers are completely determined by the NTOs and are a product of hole charges on fragment A, q_A^h, and electron charges on fragment B, q_B^e. In more general cases, the CT numbers also encode interference effects between the different excited configurations (cf. ref. 27).

The CT numbers constitute a versatile tool and have been applied successfully for, e.g., interacting chromophores,[60] push–pull systems[31] and transition metal complexes.[61,62] However, a downside of this analysis is that it depends on the a priori definition of a fragmentation scheme. To overcome this problem and obtain a more fundamental measure of charge transfer, we compute an exciton size defined as the root-mean-square separation of electron and hole

$$d_{exc} = \sqrt{\frac{\langle \gamma_{0I} | (r_h - r_e)^2 | \gamma_{0I} \rangle}{\langle \gamma_{0I} | \gamma_{0I} \rangle}} \tag{6}$$

where the bra/ket notation refers to integration with respect to r_h and r_e.[28] The exciton size, defined in this way, is a transferable measure that provides insight into charge transfer between isolated molecules,[28] covalently bonded donor–acceptor systems,[63] as well as large conjugated π-systems.[29] Purely local excitations generally have a d_{exc} of 4 Å or less, where anything above this value indicates at least partial CT character.[5,29]

In addition we will utilise the absolute mean electron–hole separation

$$d_{he} = \left| \frac{\langle \gamma_{0I} | (r_h - r_e) | \gamma_{0I} \rangle}{\langle \gamma_{0I} | \gamma_{0I} \rangle} \right|. \tag{7}$$

The d_{he} value, which is closely related to the dipole moment, measures the distance between the centroids of the hole and electron distributions. In the present context, d_{he} vanishes if both D units are equally involved in the excitation and only becomes significantly different from zero if there is a localisation of the excitation on one of them. It is, therefore, an ideal tool to monitor symmetry breaking in the excited state.

2.2 Computational details

Computations are performed on **Cz-BDT**, **Cz-AQ**, **Cz-BDT-SO$_2$** and **Cz-BDF** as shown in Fig. 1. The tertiary butyl groups used to improve solubility in the experimental studies have been excluded.[4,34] Computations in this study are divided into three parts: (i) an initial optimisation of the ground state geometry, (ii) vertical excitations with different functionals, and (iii) excited-state geometry optimisations in solution.

This journal is © the Owner Societies 2021

Phys. Chem. Chem. Phys., 2021, **23**, 26135–26150 | **26137**

For step (i) the molecular geometries of **Cz-BDT** and **Cz-AQ** were optimised at the ωB97X-V/def2-SVP level of theory[64,65] and confirmed as being minimum energy structures by a vibrational analysis at the same level. For step (ii), to determine an appropriate computational method to describe the excited state character of the molecules, the first 10 vertical excitations are first computed at the ri-ADC(2) level,[66] using the def2-TZVP basis set.[65,67] The first 10 excited states are, then, recomputed using five different density functionals with TD-DFT in the Tamm–Dancoff approximation (TDA).[68] The TDA is used here and in all following computations considering that the TDA is expected to reduce problems associated with triplet instabilities.[69] The density functionals evaluated are PBE,[70] PBE0,[71] ωPBEh,[72] CAM-B3LYP,[73–75] and ωB97X-V,[64] with the def2-SV(P)[65] basis set. In the case of ωPBEh, we used a range separation parameter of ω = 0.1 a.u. and a global amount of Hartree–Fock exchange of 20% following previous experience on related donor/acceptor systems.[52]

The ωPBEh/def2-SV(P) level of theory is selected for step (iii) based on results from density functional benchmarking to the experimental absorption maximum and the ri-ADC(2) state characters. A tuned value of ω = 0.040 a.u. is used for these calculations. The ground state (S_0) structures of all four molecules were optimised using spin-restricted Kohn–Sham DFT (RKS) along with the ωPBEh functional in toluene solution (ε = 2.3741) using a conductor-like polarisable continuum model (PCM).[76,77] Excited singlet states (S_1) were optimised using time-dependent density functional theory (TDDFT) along with the ωPBEh functional using a toluene solvent model (ε = 2.3741, ε_∞ = 2.2403) using a linear response (LR-PCM)[78,79] approach for excited-state solvation. Excited-triplet states (T_1) were optimised at the TDDFT/LR-PCM level of theory along with additional ground-state spin-unrestricted Kohn–Sham DFT computations (UKS/PCM). No empirical dispersion correction is used as there is no clear way of choosing appropriate parameters for a manually adjusted functional and since preliminary observations showed that dispersion only has a minor effect on these linear molecules.

Based on the S_0 optimised geometries, we compute the TDDFT vertical excitation energies of the first 7 excited states using two different solvation methods, LR-PCM and a perturbative state-specific solvation model (pt-SS).[19,80] At the excited-state geometries we perform TDDFT computations using the LR-PCM and SS-PCM[18,80,81] models. Specifically, the following workflow is used: all three PCM approaches start with a RKS/PCM ground-state calculation. LR-PCM, which is the default approach, proceeds with a TDDFT computation including a correction for non-equilibrium solvation added directly to the TDDFT response matrix. The ptSS approach, on the other hand, starts with a zeroth order TDDFT response matrix – not including any corrections for solvation. It proceeds by computing a state-specific correction term based on the zeroth order response vector and the relaxed ground state density. Oscillator strengths (f) for ptSS were computed as $f = 2/3 \times \Delta E \times \mu^2$ by combining the original transition dipole moments μ with the perturbatively corrected excitation energies ΔE. Finally, SS-PCM is technically carried out *via* two subsequent TDDFT jobs. In the first step the solvent field is fully equilibrated to the state of

interest and for technical reasons the optical dielectric constant ε_∞ is set to 1. In the second step the DFT orbital optimisation as well as TDDFT are carried out in the equilibrated solvent field using again ε = 2.3741 and ε_∞ = 2.2403. SS-PCM vertical emission energies were computed as the difference between the SCF energy of the first step and the total excited-state energy of the second step.

All (TD)DFT computations were performed with Q-Chem 5.2.[82] ri-ADC(2) computations used Turbomole 7.2.[83] Wavefunction analysis, following the ideas outlined in Section 2.1, were carried out in TheoDORE 2.3.[56,58]

The underlying research data (molecular geometries, input/output files of Q-Chem and Turbomole) is provided *via* a separate repository.[84]

3 Results

3.1 Molecular structures and frontier orbitals

The D–π–A–π–D molecules studied here are comprised of carbazole (**Cz**) donor units, phenylene (**Ph**) ring π bridges, and the acceptor core (**BDT** or **AQ**). These molecules have a significant degree of conformational flexibility because rotation is possible around the carbazole–phenyl bonds and the phenyl–core bonds. This gives rise to four independent dihedral angles, denoted as θ_1 / θ_1' and θ_2 / θ_2' (see Fig. 1). To restrict the associated number of conformers, we will consider only molecules of C_2 symmetry $\left(\theta_1 = \theta_1', \theta_2 = \theta_2'\right)$ and C_i symmetry $\left(\theta_1 = -\theta_1', \theta_2 = -\theta_2'\right)$. Furthermore, we find that the energy difference between the C_i and C_2 conformers is negligible (see Table S1, ESI†) indicating that both, along with other conformers, should be present at room temperature. To obtain consistent results, we select C_2 conformers for all subsequent calculations, unless specified explicitly.

Optimised ground-state geometries, considering the C_2 case, are presented in Fig. 2 and the geometric data for C_2 and C_i are shown in Table 1. Generally speaking, we find significant
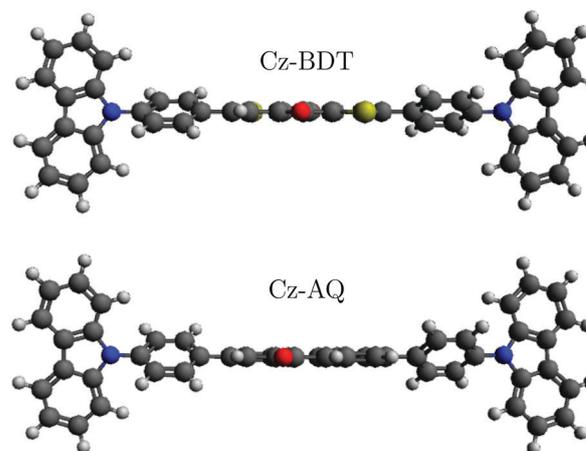

Fig. 2 The 3D structures of **Cz-BDT** and **Cz-AQ** optimised at the ωB97X-V/def2-SVP level of theory in C_2 symmetry.

26138 | *Phys. Chem. Chem. Phys.*, 2021, **23**, 26135–26150

This journal is © the Owner Societies 2021

Table 1 Twist angles (θ_1, θ_1', θ_2, θ_2' in degrees) and bond distances (d_1, d_1', d_2, d_2' in Å) for the **Cz-BDT** and **Cz-AQ** molecules obtained at the ωB97X-V/def2-SVP level of theory. Computational results from ref. 34 and 4 are shown for comparison

	Molec.	θ_1/θ_1'	d_1/d_1'	θ_2/θ_2'	d_2/d_2'
C_2 data	**Cz-BDT**	56.5	1.417	26.0	1.479
C_i data		56.7	1.417	29.9	1.479
Ref. 34		50	1.415	24	1.470
C_2 data	**Cz-AQ**	57.6	1.418	38.7	1.491
C_i data		57.2	1.418	38.1	1.491
Ref. 4		50	1.412	36	1.490

twisting for both torsion angles considered. Starting with the discussion of the C_2 geometries, the **Cz/Ph** twisting angles $\left(\theta_1/\theta_1'\right)$ are consistently $\approx 57°$ for both molecules. By comparison, the twisting around the **Ph**/core junction $\left(\theta_2/\theta_2'\right)$ is notably reduced owing to reduced steric hindrance. Twisting in **Cz-AQ** is larger than in **Cz-BDT** ($39°$ *vs.* $26°$) which can be understood by considering that the **AQ** group has two hydrogen atoms in the vicinity of the **Ph** group whereas **BDT** only has one. **Cz-BDT** is, thus, expected to allow for enhanced conjugation between the **Ph** and **BDT** groups and we will explore the consequences of this on the observed photophysics in more detail below. Proceeding to the bond distances, we find that the **Cz–Ph** distances $\left(d_1/d_1'\right)$ are very similar for both molecules (≈ 1.417 Å). For the d_2/d_2' values however, the bond distance is shorter in **Cz-BDT** (1.479 Å) than **Cz-AQ** (1.491 Å) following the same trends as expected for the bond angles, *i.e.* conjugation is stronger for **Cz-BDT**. Table 1 also presents results for the C_i geometry as well as data from previous work on the two molecules[4,34] using the B3LYP functional. The observed trends between the three data sets are consistent indicating that these geometric parameters are fairly robust with respect to both the precise conformer studied and the functional chosen.

To discuss the electronic structure of this system, we start with the frontier molecular orbitals as is usually done for these types of molecules. The highest occupied molecular orbital (HOMO) and lowest unoccupied MO (LUMO) for **Cz-BDT** are shown in Fig. 3, and for **Cz-AQ** in Fig S1 (ESI†). The HOMO and
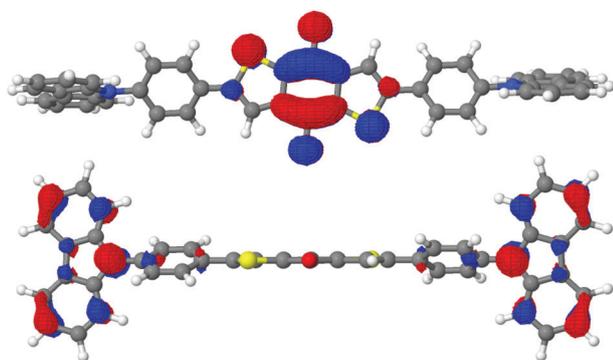

Fig. 3 The HOMO (bottom) and LUMO (top) for **Cz-BDT** calculated at the ωB97X-V/def2-SVP level of theory.

LUMO look the same for both molecules; the HOMO is located on the carbazole donor units and the LUMO is located on the acceptor core and there are only negligible contributions on the bridging **Ph** units. A transition from the HOMO to the LUMO would, therefore, produce an excited state with a large amount of charge transfer (CT) character, shifting electron density from the donor to the acceptor. However, HOMO/LUMO plots can only ever provide a very rough picture of the electronic structure and we will proceed to a detailed analysis of the excited states and all orbitals involved, below.

3.2 Vertical excitations

Proceeding to the excited states of **Cz-BDT** and **Cz-AQ**, we first endeavour to find a computational method that describes their states accurately. To do so, we consider experimental results as well as reference calculations at the *ab initio* ri-ADC(2)/def2-TZVP level of theory. Experimental results are presented in Table 2. **Cz-BDT** is found to have an absorption maximum at 2.65 eV and a strongly red-shifted emission at 1.87 eV. In the case of **Cz-AQ** both values are about 0.3 eV higher. Table 2 also highlights the considerable difference of the fluorescence quantum yield Φ measured in solution between the two molecules, showing a more than six-fold drop when going from **Cz-AQ** to **Cz-BDT**. Whereas, the shift in absorption and emission maxima can be explained by the lowering of the LUMO, it is harder to gain understanding of the drop in quantum yield and we will endeavour to study this in detail.

To obtain computational reference data, we compute the first ten excited states of **Cz-BDT** and **Cz-AQ** at the ri-ADC(2) level in gas phase at the ground state C_2 geometries. To show the results of these computations, we use a graphical representation, developed in ref. 30 and 56, that provides compact information about excited energies and characters based on the CT numbers [eqn (2)] and the natural transition orbitals [eqn (3)]. For the CT number analysis, the molecule is first divided into different fragments. In the case of **Cz-BDT**, these are (i) the **Cz** donors, (ii) the phenylene (**Ph**) bridges, (iii) the **BDT** core, and (iv) the oxygen groups on the core. Using these fragments, we can now decompose the excited states into different contributions as shown in Fig. 4(a). We will consider the following five contributions:

- **Cz** → **BDT** charge transfer (red),
- **Ph** → **BDT** charge transfer (green),
- local **BDT** excitations (blue),
- excitations from the oxygen atoms to **BDT** indicating nπ* character (orange), and
- excitations within the **Cz** and **Ph** units (purple).

Table 2 Experimentally measured photophysical data for **Cz-BDT** and **Cz-Aq**: energies for the first absorption and emission maxima ($E_{abs,max}$, $E_{em,max}$) and photoluminescence quantum yield (Φ)

	$E_{abs,max}$ (eV)	$E_{em,max}$ (eV)	Φ
Cz-BDT[a]	2.65	1.87	0.095
Cz-AQ[b]	2.91	2.22	0.60

[a] Ref. 34, measured in toluene. [b] Ref. 4, measured in toluene.

This journal is © the Owner Societies 2021

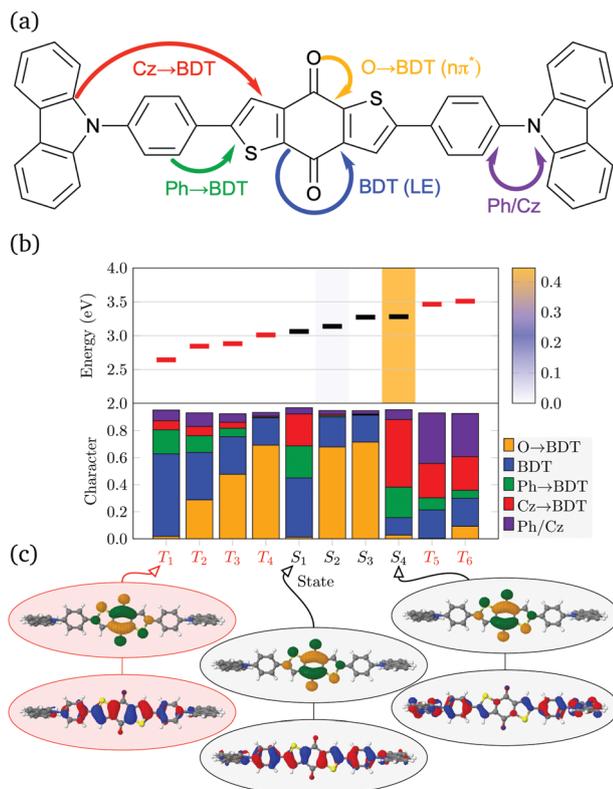*Phys. Chem. Chem. Phys.*, 2021, **23**, 26135–26150 | **26139**

Fig. 4 Analysis of excited states in **Cz-BDT** at the ri-ADC(2)/def2-TZVP level of theory: (a) Schematic of the fragment based decomposition, (b) excited state energies for singlets in black and triplets in red with oscillator strengths as shading (top) and characters (bottom) of the first ten excited states of **Cz-BDT**, and (c) natural transition orbitals (NTOs) for selected states.

These are shown schematically in Fig. 4(a) and a detailed definition of the different contributions is given in Fig. S2 (ESI†). Any excited state is a combination of these elementary contributions in varying weights and we will use bar graphs to represent the composition of the individual states.

The excitation energies for **Cz-BDT** are presented in the upper panel in Fig. 4(b) showing that this molecule possesses four low-energy triplet states (red) before the first singlet state (black). Viewing the lower panel of Fig. 4(b), we find that T_1 is dominated by local $\pi\pi^\star$ character on the **BDT** core, represented in blue, with smaller **Ph** $\rightarrow$ **BDT** CT contributions (green). The corresponding NTOs are shown in panel (c) highlighting that the hole NTO (shown in blue/red) is a π-orbital on **BDT** with some contributions on the **Ph** bridge whereas the electron NTO (shown in green/orange) is a $\pi^\star$-orbital located right at the centre of **BDT** resembling the LUMO shown in Fig. 3. Proceeding to the next three triplet states, we find that these are a mixture of local $\pi\pi^\star$ character on **BDT** (blue) and $n\pi^\star$ character (orange) with increasing $n\pi^\star$ character from T_2 to T_4. The first singlet state (S_1) lies just above 3.0 eV and is similar in character to T_1 albeit with more charge transfer character (red and green). This is also reflected by the dominant hole NTO, shown at the bottom in panel (c), which has extended contributions on the **Ph** bridges. The vertical gap between T_1 and S_1 is calculated to

be 0.42 eV. The S_2 and S_3 states are locally excited states dominated by $n\pi^\star$ character. The S_4 state lying at 3.28 eV is a CT state which contains significant **Cz** $\rightarrow$ **BDT** character (red). For the T_5 and T_6 states, we find a mixture of state characters with roughly 40% of the excitation character attributed to local excitations on **Ph** and **Cz**.

Reviewing the states in the canonical orbital picture, we find that all states go predominantly into the LUMO, with only the T_5 and T_6 states also containing significant contributions into higher virtual orbitals (LUMO+1 and LUMO+3). Conversely, the HOMO only plays a minor role for the low energy states and of all the states considered here, only S_1 and S_4 and none of the triplet states have notable HOMO–LUMO character (62% for S_1, 85% for S_4). This highlights that a simple visualisation of the HOMO and LUMO can by no means explain the photophysics of complicated TADF systems as studied here.

The oscillator strengths are represented *via* the colour shading in the upper panel of Fig. 4(b). At the highly symmetric geometry shown, the first bright state is S_4 at 3.28 eV, with an oscillator strength of 0.45. The lowest $\pi\pi^\star$ state, S_1 at 3.06 eV, possesses vanishing oscillator strength within the computation. This can be understood by the fact that the analogous state is symmetry forbidden under C_i symmetry and by assuming that similar orbital interactions are also present at the C_2 geometry. However, once the symmetry is broken, this state is expected to borrow intensity from the bright state suggesting that this state contributes to the lowest energy band in the absorption spectrum, which is found experimentally at 2.65 eV.

Next, we move to the second molecule studied here, **Cz-AQ**. As opposed to **Cz-BDT** where the lowest state was of local $\pi\pi^\star$ character, we find in the case of **Cz-AQ** that the first three states (S_1, T_1, T_2) are all of $n\pi^\star$ character (orange). The calculated vertical gap between S_1 and T_1 is 0.32 eV which is 0.1 eV smaller than found in **Cz-BDT**. The T_3 and T_4 states are mixed in character, with mostly local contributions on **AQ** and smaller amounts of charge transfer from **Ph** and **Cz** to the core. The S_2 state is an $n\pi^\star$ state. S_3 and S_4 are both described as charge transfer states with significant **Cz** $\rightarrow$ **BDT** character. Only S_4 has an appreciable oscillator strength, which can, again, be understood in terms of symmetry properties. The S_4 excitation energy is 3.55 eV which is 0.64 eV higher than the experimentally determined absorption maximum, thus ri-ADC(2) overestimates the energy of the bright state by about 0.5 eV for both **Cz-BDT** and **Cz-AQ**. Conversely, ri-ADC(2) is expected to underestimate the energies of $n\pi^\star$ states and CT states by a few tenths of an eV.[8,85,86] Nonetheless, we believe that ri-ADC(2) provides a good reference for the expected state characters involved. In particular, these results indicate that all types of states, *i.e.*, local $\pi\pi^\star/n\pi^\star$ states and CT states, play a role.

Finally, viewing the difference between Fig. 4 and 5, we find that the S_1 and T_1 states of **Cz-BDT** have significant locally excited $\pi\pi^\star$ contributions on **BDT** whereas S_1 and T_1 are dominated by $n\pi^\star$ character for **Cz-AQ**. Proceeding to the higher excited states, we find enhanced CT (red) for **Cz-AQ**. Thus, we can already anticipate that the photophysics of **Cz-AQ** will be dominated by its CT states whereas locally excited $\pi\pi^\star$ contributions are more important for **Cz-BDT**.

26140 | *Phys. Chem. Chem. Phys.*, 2021, **23**, 26135–26150
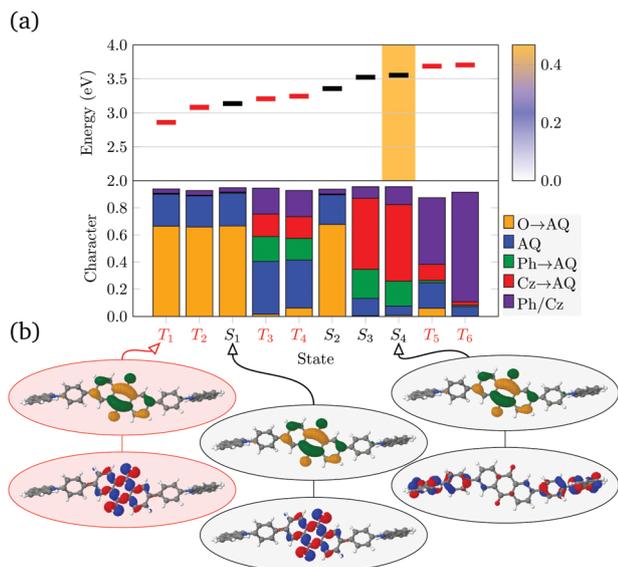
This journal is © the Owner Societies 2021

Fig. 5 Analysis of excited states in **Cz-AQ** at the ri-ADC(2)/def2-TZVP level of theory: (a) excited state energies for singlets in black and triplets in red with oscillator strengths as shading (top) and characters (bottom) of the first ten excited states of **Cz-BDT**, and (b) natural transition orbitals (NTOs).

Having described the states at the *ab initio* ri-ADC(2) level, it is of interest whether an approximate density functional can be used with the aim of both saving computational time, and to find a method that matches closer with experimental absorption wavelengths. For this purpose, the first five singlet and triplet

states for **Cz-BDT** and **Cz-AQ** are calculated using TDDFT with the PBE, PBE0, ωPBEh, CAM-B3LYP and ωB97X-V functionals. Fig. 6 and Fig. S3 (ESI†) contain the results for **Cz-BDT** and **Cz-AQ** respectively, with the state characters assigned as explained in Fig. 4(a). The experimental absorption maximum is shown as a dashed orange line. The exciton size (d_{exc}) for the excited state [eqn (6)], an alternative measure for charge transfer,[28,29] is shown in the bottom panel. In Fig. 6 the functionals are arranged according to an effective increase in Hartree–Fock exchange from left to right: PBE (0%), PBE0 (25%), ωPBEh (20–100%, ω = 0.1 bohr^{-1}), CAM-B3LYP (19–65%, μ = 0.33 bohr^{-1}) and ωB97X-V (16-100%, ω = 0.3 bohr^{-1}) where the amount of Hartree–Fock exchange (HFX) and the range-separation parameter (ω/μ) are given in parentheses. Overall, with increasing HFX we find that the state energies, vertical singlet–triplet gaps, and the oscillator strengths of bright states increase.

More strikingly, the middle panel in Fig. 6 reveals the dramatic difference in the state characters obtained with the different functionals. In the case of PBE on the left, the first 8 states are almost entirely of **Cz → BDT** CT character (red). By contrast, any substantial CT is missing for ωB97X-V on the right. Only the three functionals in the middle contain the mixture of local $\pi\pi^*/n\pi^*$ states and CT states as found for ri-ADC(2). The same trend is also found for the exciton sizes in the lower panel. The first eight states for PBE show enhanced charge separation (d_{exc} > 10 Å) whereas no state with an exciton size above 6 Å is found for ωB97X-V. And, again, more diverse values are found for the functionals in between. The difference in state character is reflected by changes in oscillator strength, shown as shading
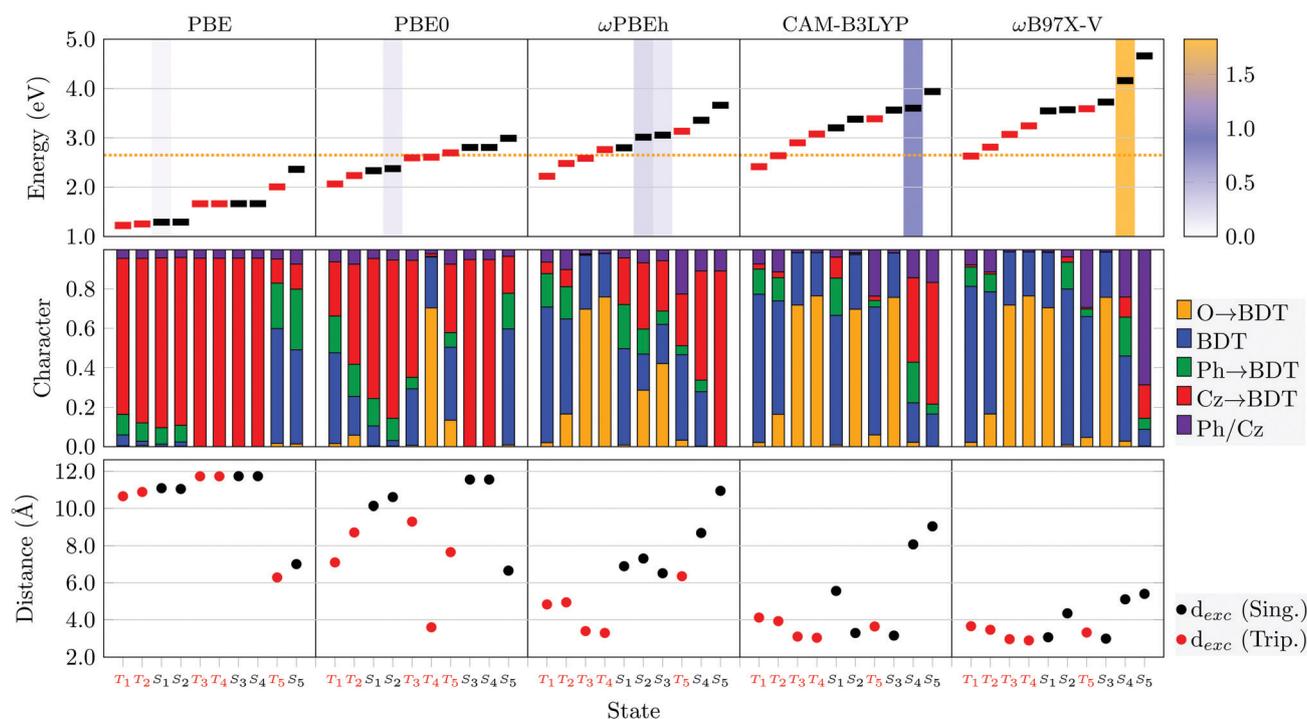

Fig. 6 Analysis of the first five singlet and triplet states of **Cz-BDT** in C_2 symmetry computed using five different functionals (displayed in the top row) in vacuum. Top: Excited-state energies (singlets black, triplets red) along with the experimental absorption maximum as dotted orange line and oscillator strengths shown as shading; middle: excited-state characters; bottom: exciton size d_{exc}.

in the top panel of Fig. 6, which is strongly increased for the functionals with more HFX. These differences highlight the charge transfer problem in TDDFT showing that varying amount of HFX does not only affect the energies[13,87] but also excited-state properties.[29,88] It is noteworthy, here, that a larger amount of "exact" exchange does not necessarily produce better agreement with higher-level computational methods considering that a reduced amount of exchange corresponds to a physically meaningful screened Coulomb interaction, *cf.* ref. 5.

We proceed to detailed results for the individual functionals. For PBE we find two sets of four almost degenerate CT states (two singlets and two triplets). These can be understood in the sense that they are composed of independent **Cz → BDT** transitions on the left and right hand side of the molecule, which are effectively decoupled and neither split *via* Coulomb nor exchange interactions. The exciton sizes are all above 10 Å, which is similar to the distance from the centre of the **Cz** donor to the centre of the **BDT** acceptor highlighting that charge transfer between them dominates with no intermediate locally excited contributions playing a role. Considering the global hybrid PBE0, we still find significant amounts of CT character for the first four states but there is already much more structure when compared to PBE. In particular, it is found that the T_1 state has enhanced local character (blue) and an associated reduction in exciton size to 7.1 Å. Moving to ωPBEh, we find that the first four states are triplets of local $\pi\pi^*$ and $n\pi^*$ character. These are followed by three singlet states around 3 eV with a mixture of local $\pi\pi^*$ and $n\pi^*$ as well as CT character. We find two bright states at 3.01 and 3.06 eV, which possess significant amounts of, both, $n\pi^*$ and CT character. This should be understood in the sense that there is an accidental degeneracy between an $n\pi^*$ and CT state, producing this mixing. Moving to the remaining two functionals, we find that the first state with appreciable CT character is above 3.5 eV for CAM-B3LYP and no CT state is found at all for ωB97X-V within the energy window considered (up to 4.5 eV).

For **Cz-AQ** (Fig. S3, ESI†), we find broadly the same story: PBE and PBE0 overestimate the amount of CT character of the lowest lying states and underestimate the energy of the bright state, while ωB97X-V underestimates the CT character and severely overestimates the energy of the bright state. The main differences between ωPBEh and CAM-B3LYP are the energy of the bright singlet CT state, with ωPBEh providing a better value relative to the experimental absorption maximum, and the ordering of the states with respect to the state character. With the ωPBEh functional, we find a similar mixture of local $\pi\pi^*/n\pi^*$ and CT states as for ri-ADC(2). The only difference is that the relative energies of the $n\pi^*$ states are somewhat raised yielding a different ordering of the dark low-energy states. However, as discussed above, ri-ADC(2) is expected to slightly underestimate $n\pi^*$ state energies, thus supporting the description by ωPBEh.

For both **Cz-BDT** and **Cz-AQ**, the ωPBEh functional gives a vertical excitation energy for the lowest bright state at a value in close proximity to the experimental value (indicated as dotted orange line in Fig. 6 and Fig. S1, ESI†). Here, experience

suggests that due to vibronic effects, the vertical excitation should be about 0.1 eV above the experimental maximum,[89] therefore indicating excellent agreement of the computed values. Furthermore, ωPBEh succeeds in describing the state characters of the low-energy states involved when compared to the higher-level ri-ADC(2) method and is expected to capture the overall photophysics well. Therefore, we will proceed by using the ωPBEh functional in the further course of the study.

3.3 Excited state minima and solvation

Having described the vertical excitations and identifying ωPBEh as a method for providing the overall excited state characters effectively, we now turn to an analysis of the excited state minimum geometries in solution for **Cz-BDT** and **Cz-AQ**. Before proceeding, we aim at fine tuning the range separation parameter ω.[90,91] For this purpose, we use the equation

$$J = \sqrt{(\varepsilon_{HOMO} + IP)^2 + (\varepsilon_{LUMO} + EA)^2} \qquad (8)$$

where ε_{HOMO} and ε_{LUMO} are the HOMO and LUMO energies of the neutral system, and IP and EA are the ionisation potential and electron affinity. The optimum value of ω is found by minimising J. Results of J as a function of ω for **Cz-BDT** and **Cz-AQ** are presented in Fig. 7 considering computations in toluene solvation and in vacuum. The values between the two molecules are very similar but striking differences are found when comparing results in solution and in vacuum. In solution, the optimal ω value is 0.04 a.u. whereas in gas phase a value of 0.15 a.u. is obtained. In the following, we will use the solution value (ω = 0.04 a.u.) whereas calculations using enhanced Hartree–Fock exchange (ω = 0.10 a.u.) are shown in the ESI† (Fig. S4–S6). In Section 4.1, we will review the main results using both ω values.

First, the geometries of the S_0, S_1, and T_1 minima are optimised using ωPBEh/def2-SVP within toluene solvation, considering that toluene was used in the experimental studies.[4,34]
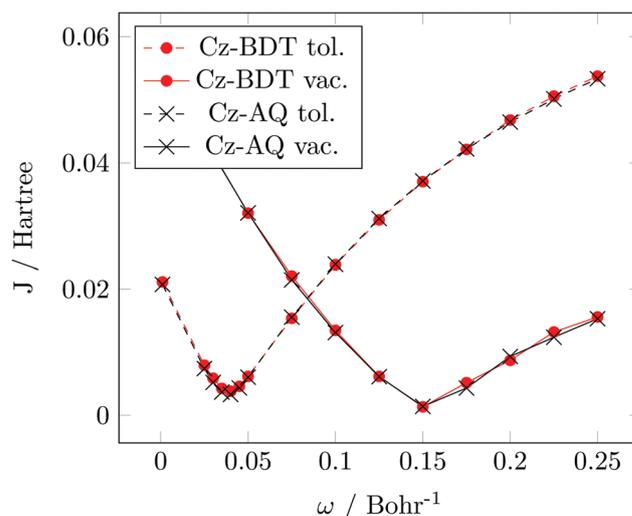

Fig. 7 Optimal tuning procedure for the ωPBEh functional applied to **Cz-BDT** and **Cz-Aq** in toluene solution (dashed lines) and vacuum (solid lines).

26142 | *Phys. Chem. Chem. Phys.*, 2021, **23**, 26135–26150

This journal is © the Owner Societies 2021

Table 3 Geometric parameters for **Cz-BDT** and **Cz-AQ** obtained at the ωPBEh/def2-SVP level of theory with a toluene PCM solvent model. Only symmetry-unique values are given

Molecule	Geometry	Method	θ_1/θ_1'	d_1/d_1'	θ_2/θ_2'	d_2/d_2'
Cz-BDT						
	S_0 min	RKS	−54.1	1.411	−14.9	1.465
	S_1 min	TDDFT	−50.3	1.408	4.9	1.458
	T_1 min	TDDFT	−47.9	1.402	3.3	1.446
	T_1 min	UKS	−47.9	1.402	3.3	1.445
Cz-AQ						
	S_0 min	RKS	−54.1	1.412	−31.8	1.481
	S_1 min	TDDFT	−58.1/−53.6	1.418/1.416	−31.3/−31.0	1.483/1.481
	T_1 min	TDDFT	−43.9/−58.2	1.391/1.416	8.2/35.2	1.452/1.481
	T_1 min	UKS	−48.5	1.403	20.6	1.465

The S_1 is always optimised with TDDFT whereas, following ref. 8, 17 and 92, we investigate two possibilities for optimising the T_1 minimum, an excited-state optimisation using TDDFT and a formal ground-state optimisation using UKS. The key structural parameters obtained from these optimisations are outlined in Table 3, and the geometries are shown in Fig. 8. For BDT, we find that upon excitation it planarises, *i.e.* dihedral angles become smaller, that the interring distances become shorter, and that the molecule retains its symmetry. Variations in the **Cz-Ph** torsion θ_1/θ_1' are relatively minor whereas the θ_2/θ_2' values become close to zero for S_1 and T_1. This means that the **Ph-BDT-Ph** system becomes almost planar after photo-excitation, see also Fig. 8, effectively producing one extended π-system, and we will revisit this point below. For **Cz-AQ**, on the other hand, we find pronounced symmetry breaking in the TDDFT computations as evidenced by the variations in the two torsion angles (θ_1/θ_1' and θ_2/θ_2'). Generally speaking, the torsion angles remain at larger absolute values when compared to **Cz-BDT**. Interestingly, when we perform the optimisation using UKS, no symmetry breaking is observed here.

We proceed by discussing the excited states at the individual geometries. For this purpose, we consider two different approaches, the standard LR-PCM method also used for the TDDFT optimisations, as well as a more involved state-specific

approach, which is expected to provide an improved description of CT states.[18,19] For the vertical absorption (S_0), we use the perturbative (ptSS) approach whereas for emission (S_1/T_1) we use the equilibrated SS-PCM approach. Starting the discussion with **Cz-BDT**, we present data for the lowest four triplet and three singlet excited states in Fig. 9. The T_1 state, located at 1.81 eV, is dominated by local BDT character whereas the next four states (T_2, S_1, S_2, T_3) have enhanced CT character (red). These are followed by an $n\pi^\star$ state (T_4) and another CT state (S_3). Using the ptSS solvation scheme leaves T_1 largely unaffected but stabilises the states with more CT character. S_1 becomes the bright state, located at only 1.94 eV, which is notably below the experimental absorption maximum of 2.65 eV. We note, here, that an ω value of 0.10 a.u. improves the absorption maximum (predicted at 2.71 eV as shown in Fig. S4, ESI†) but it does so at the cost of producing an unreasonably large singlet–triplet gap (see below).

Next, we proceed to the optimised minimum of the S_1 state. The S_1 energy is found at an adiabatic energy of 1.99 and 1.83 eV using LR-PCM and SS-PCM, respectively. The obtained emission energy is 1.71 eV, which is in reasonable agreement with the experimental value of 1.87 eV.[34] The S_1 state at the optimised geometry has a similar character to the vertical excitation, *i.e.* mixed local and CT, only that the exciton size d_{exc} of 9.65 Å (SS-PCM) is slightly reduced when compared to the ground state geometry (10.37 Å). The S_1 state retains the formal gerade symmetry present at the S_0 geometry and, therefore, has vanishing oscillator strength. An optically dark S_1 minimum with only partial CT character certainly runs counter to the initial design strategy of using a D–π–A–π–D system and may well explain the poor performance of **Cz-BDT** in TADF applications.

Proceeding to T_1, we compare data using three different methods: TDDFT/LR-PCM and TDDFT/SS-PCM at the TDDFT/LR-PCM geometry, as well as TDDFT/SS-PCM at the UKS/PCM T_1 geometry. We find that optimisation of T_1 leads to a notable stabilisation of T_1 obtaining adiabatic T_1 energies between 1.33 and 1.59 eV for the three methods. In all cases, the rather local character is retained obtaining exciton sizes just above 6 Å.

Results for geometry optimisations of the individual states for **Cz-AQ** are presented in (Fig. 10). At the S_0 minimum, we find similar state characters as for BDT only that CT character is enhanced (as seen by more pronounced red bars in the middle
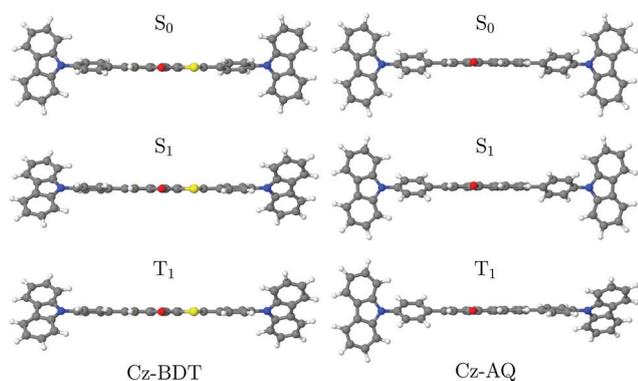

Fig. 8 The S_0, S_1 and T_1 minimum geometries of **Cz-BDT** and **Cz-AQ** optimised at the ωPBEh/def2-SVP level of theory.
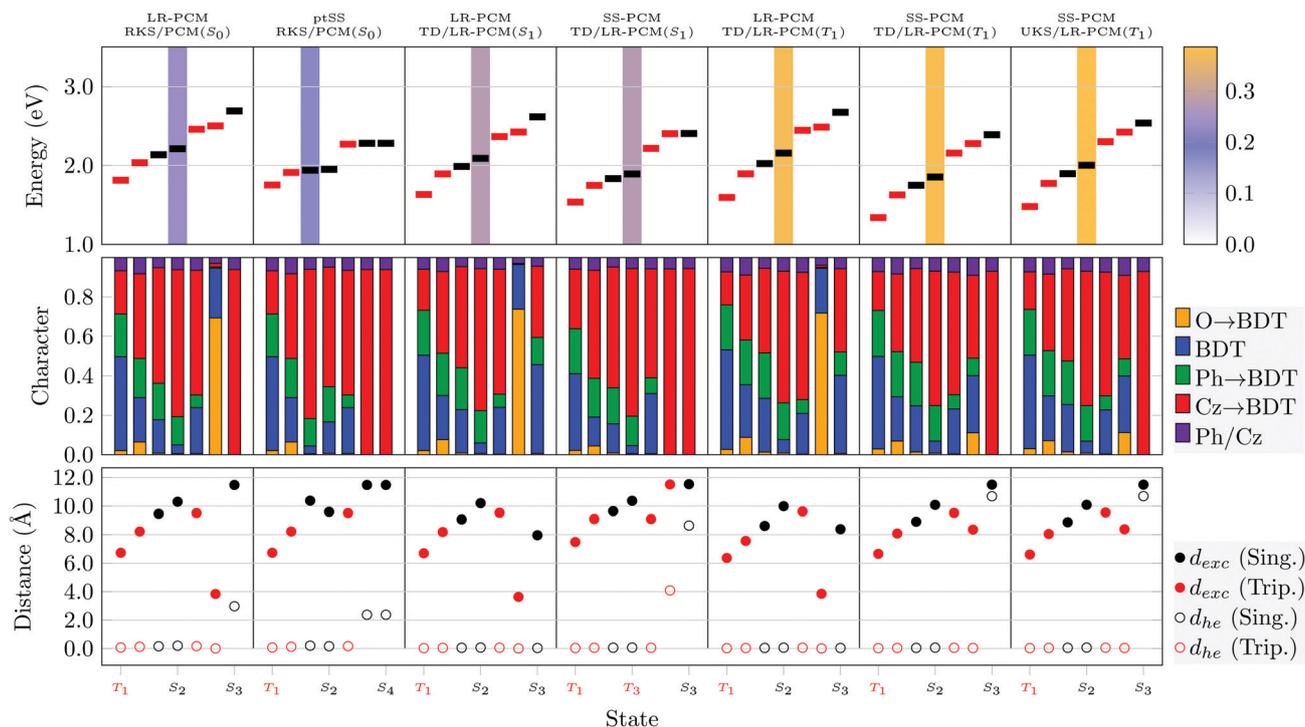
Fig. 9 Analysis of the lowest singlet and triplet states of **Cz-BDT** at the S_0, T_1 and S_1 minimum geometries: Adiabatic energies and oscillator strengths (top), excited-state characters (middle), and charge transfer measures (d_{exc}, d_{he}, bottom). The excited-state solvation model and method for computing the geometry are given in the top two lines, always in connection with the ωPBEh/def2-SVP level of theory.
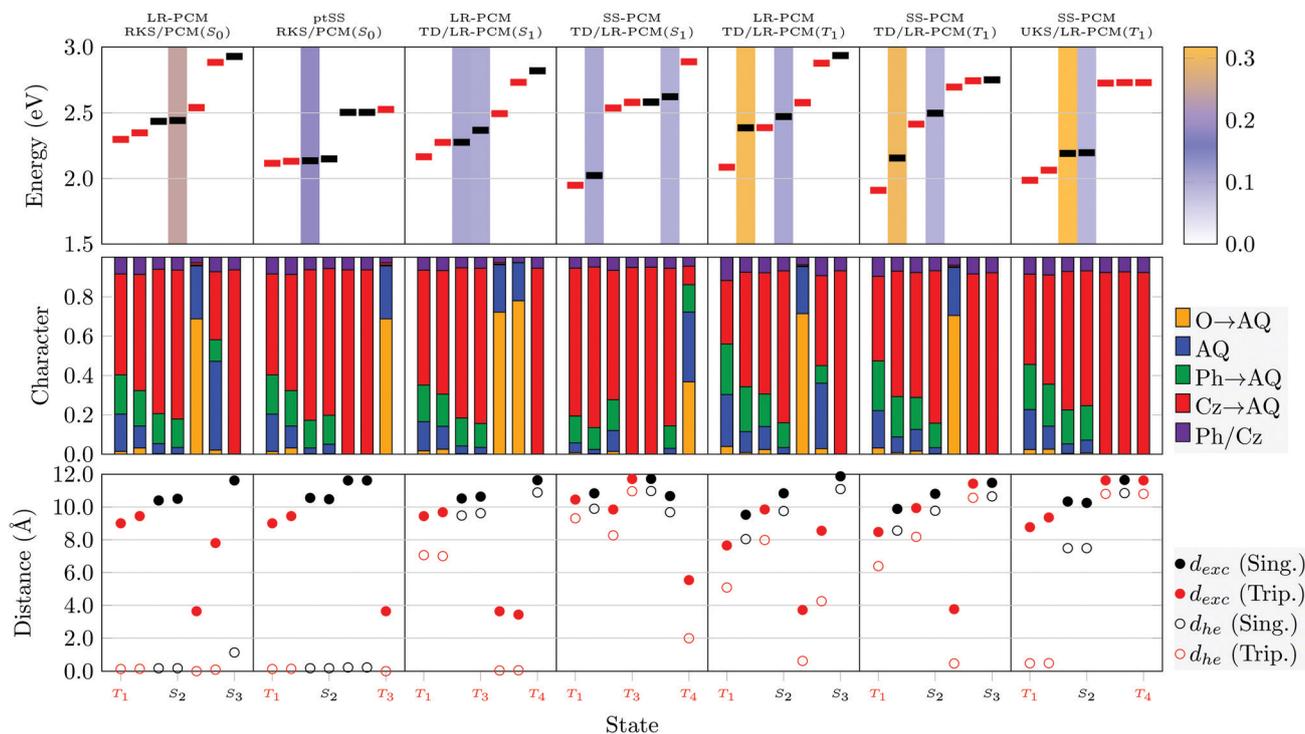

Fig. 10 Analysis of the lowest singlet and triplet states of **Cz-AQ** at the S_0, T_1 and S_1 minimum geometries: Adiabatic energies and oscillator strengths (top), excited-state characters (middle), and charge transfer measures (d_{exc}, d_{he}, bottom). The excited-state solvation model and method for computing the geometry are given in the top two lines, always in connection with the ωPBEh/def2-SVP level of theory.

panel and larger exciton sizes in the lower panel). The bright S_2 state is found at 2.44 eV, which is again notably lower than the

experimental maximum of 2.91 eV. The ptSS solvation scheme is, again, found to strongly affect the CT states. On the other hand,

26144 | *Phys. Chem. Chem. Phys.*, 2021, **23**, 26135–26150

This journal is © the Owner Societies 2021

the triplet $n\pi^{\star}$ state (T_3) is almost unaffected by the solvation. Viewing the other panels in Fig. 10, one finds that the energies but also other properties of the different states are quite strongly affected by the different geometries and solvation schemes. Crucially, we find for the TDDFT optimised S_1 geometry that the S_1 state becomes bright and has a significant amount of charge transfer character (red) along with an enhanced exciton size of 10.39 Å (SS-PCM). We propose to interpret this phenomenon in the context of excited-state symmetry breaking:[12,93] The S_1 state is Laporte forbidden at the ground state geometry due to its approximate inversion symmetry but this restriction is lifted once the symmetry is broken in the excited state as one half of the molecule planarises (see Table 3). To represent the symmetry breaking, we use the linear electron–hole separation (d_{he}, eqn (7)). This value vanishes for symmetric charge transfer systems but approaches the value of d_{exc} in the idealised case where charge is transferred from one donor to one acceptor, both represented as a point charge.[27] As expected, d_{he} is zero for the symmetric S_0-optimised geometries. In the case of S_1, by contrast, we find that for all the $\pi\pi^{\star}$ states d_{he} differs strongly from zero reaching almost the value of d_{exc}. This highlights that symmetry breaking of the geometry does indeed also localise the excited states.

The T_1 state at the T_1 geometry has enhanced local character (blue, green) and a reduced exciton size (<8 Å) when compared to S_1 at the S_1 geometry considering all three levels of theory considered. Nonetheless, pronounced symmetry-breaking occurs, which is reflected by the brightness of the S_1 state and the non-vanishing d_{he} values.

Reviewing Fig. 9 and 10, we find adiabatic singlet triplet gaps of 0.36 eV and 0.11 eV for **Cz-BDT** and **Cz-AQ**, respectively, highlighting the suitability for TADF of the latter. Furthermore, a clear difference is observed in terms of excited-state character of the optimised S_1 state. This state remains dark for **Cz-BDT** whereas it becomes a bright symmetry-broken CT state for **Cz-AQ**. The enhanced optical brightness is certainly beneficial for luminescence while also enhanced CT agrees with the underlying design strategy.

3.4 Outlook – Cz-BDT-SO2 and Cz-BDF

Having provided a detailed analysis of **Cz-BDT** and **Cz-AQ**, we will now proceed to two additional molecules, alluded to briefly in the introduction and shown in Fig. 1: (i) **Cz-BDT-SO₂** containing an oxidised derivative of the BDT acceptor, with two oxygen atoms bound to each sulfur atom; and (ii) **Cz-BDF**, the benzodifuran

derivative of BDT, where the sulfur atoms are replaced with oxygen atoms. As opposed to **Cz-BDT** and **Cz-AQ**, which have been synthesised and well-characterised, these two molecules have not yet been synthesised.

The geometric parameters for **Cz-BDT-SO₂** and **Cz-BDF**, obtained in analogy to Table 3, are listed in Table 4. Starting with the S_0 state of **Cz-BDT-SO₂**, we find that its **Cz/Ph** torsion angles $\left(\theta_1 / \theta_1'\right)$ are similar to the previous two molecules whereas the core/**Ph** torsion angles $\left(\theta_2 / \theta_2'\right)$ are significantly reduced indicating that the central **Ph**–core–**Ph** system is almost planar. Excitation into S_1 induces pronounced symmetry breaking with one of the **Cz**-core angles (θ_1) almost reaching 90°. In addition, the θ_2 / θ_2' angles are slightly increased, which is the opposite trend to what was seen for **Cz-BDT**. Excitation into T_1 only causes minor alterations in the geometry. Proceeding to **Cz-BDF**, we find that this molecule stays symmetric and fairly rigid in all states considered possessing a largely planar central **Ph**–core–**Ph** system. Finally, it is interesting to note that for all four molecules in this work, the bond distances change with the twisting angles. An increase/decrease in θ leads to an increase/decrease in d showing that the effect of enhanced conjugation produced by a smaller torsion angle also affects the bond distances.

An analysis of the excited states of **Cz-BDT-SO₂** and **Cz-BDF** at their S_0, S_1, and T_1 optimised geometries in solution is presented in Fig. 11. The data shown is analogous to Fig. 9 and 10 with the exception that we only present results using the higher-level state-specific solvation models here. Starting with **Cz-BDT-SO₂**, shown on the left in Fig. 11, we find that the excitation energies are significantly reduced when compared to **Cz-BDT** with all seven calculated excited states at or below 1.5 eV in the ptSS scheme at S_0 geometry. All states possess notable amounts of CT character (red bars) and exciton sizes above 8.0 Å, their CT character slightly enhanced when compared to **Cz-BDT**. The S_1 is found to be a CT state with predominant **Cz** → core contributions located at 1.21 eV possessing an oscillator strength of 0.553. The following three states (T_3, S_2, S_3) are found to possess almost pure **Cz** → core character (red). These latter states show clear symmetry breaking as indicated by the d_{he} values in the lower panel despite the near symmetric structure of the molecule.

Optimisation of **Cz-BDT-SO₂** in the S_1 state strongly stabilises the CT states. The S_1 and T_1 are both of almost pure **Cz** → core character and almost degenerate. The vertical emission energy

---

Table 4 Geometric parameters for **Cz-BDT-SO₂** and **Cz-BDF** obtained at the ωPBEh/def2-SVP level of theory with a toluene PCM solvent model. Only symmetry-unique values are given

Molecule	Geometry	Method	θ_1 / θ_1'	d_1 / d_1'	θ_2 / θ_2'	d_2 / d_2'
Cz-BDT-SO₂						
	S_0 min	RKS	−48.6	1.402	4.1/4.0	1.445
	S_1 min	TDDFT	−89.3/−56.5	1.435/1.415	15.4/16.9	1.462/1.459
	T_1 min	TDDFT	−47.9/−48.0	1.401/1.402	4.1/4.0	1.443/1.444
Cz-BDF						
	S_0 min	RKS	−54.3	1.411	−2.8	1.455
	S_1 min	TDDFT	−49.5	1.407	4.1	1.448
	T_1 min	TDDFT	−47.7	1.402	3.2	1.438

This journal is © the Owner Societies 2021

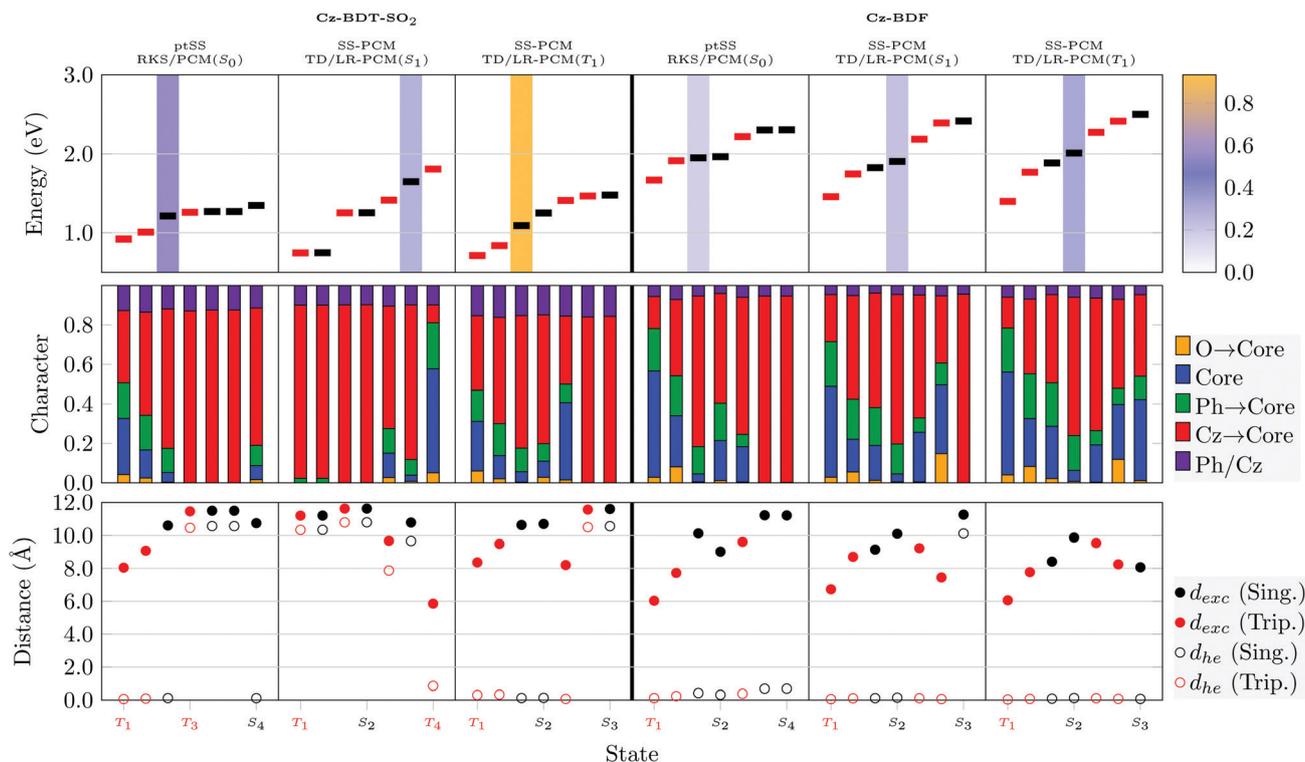*Phys. Chem. Chem. Phys.*, 2021, **23**, 26135–26150 | **26145**

Fig. 11 Analysis of the lowest singlet and triplet states of **Cz-BDT-SO₂** (left) and **Cz-BDF** (right) at the S_0, T_1 and S_1 minimum geometries: adiabatic energies and oscillator strengths (top), excited-state characters (middle), and charge transfer measures (d_{exc}, d_{he}, bottom).

from these computations (ω = 0.04 a.u.) comes out at 0.44 eV whereas the emission energy for ω = 0.10 a.u. is 1.41 eV. Optimisation of T_1 produces a more local T_1 lying at almost the same energy as T_1 and S_1 at the S_1-geometry. More generally, the lower lying states have a similar appearance to the S_0-minimum with mixed local and CT character.

The excited states of **Cz-BDF** (Fig. 11, right) bear resemblance to those of **Cz-BDT** (Fig. 9). At the S_0 geometry two mixed local/CT triplet states are found before S_1, which is dominated by CT character and bright. S_1 is found at 1.95 eV, which is almost equivalent to **Cz-BDT**. All remaining states are dominated by CT character (red) and possess exciton sizes above 8 Å. Optimisation of S_1 slightly lowers its adiabatic energy (from 1.95 eV to 1.83 eV) yielding an emission energy of 1.69 eV. The S_1 and S_2 states remain almost degenerate only that S_2 becomes the bright state, here. Optimisation of T_1 slightly stabilises the energy of this state inducing an adiabatic singlet–triplet gap of 0.43 eV. Otherwise, the states remain largely unaffected.

4 Discussion

Before concluding, we want to summarise and discuss the results, presented above, in the context of three specific issues: (i) the overall photophysics of the molecules studied, (ii) general differences in singlet and triplet state wavefunctions and their relevance in terms of photophysics and computational modelling, and (iii) further methodological aspects concerned with the density functionals and solvation models used.

4.1 Summary of the photophysics

A summary of the key photophysical data for the four molecules is presented in Table 5. Here, we consider our highest level results, *i.e.*, absorption energies at the TDDFT/ptSS level and emission energies using TDDFT/SS-PCM all with the ωPBEh functional. Two different values for the range-separation parameter ω are contrasted: (i) a value of ω = 0.040 a.u., the optimal value in solution and used for the above discussion, and (ii) a value of ω = 0.100 a.u., which is about the average between the values optimised for solution and gas phase (*cf.* Fig. 7). We find that an ω value of 0.100 a.u. works well in reproducing the absorption maxima of **Cz-BDT** and **Cz-AQ** whereas their energies are underestimated for ω = 0.040 a.u. Also the emission maxima of both molecules are reproduced more accurately with ω = 0.100 a.u. On the other hand, this larger ω value produces an unreasonably large adiabatic singlet–triplet gap ($\Delta E_{ST,ad.}$), above 0.5 eV, which would render TADF almost impossible. Literature values for $\Delta E_{ST,ad.}$ are not available for any of the molecules studied here but, using the data from ref. 4, we can estimate the adiabatic gap of **Cz-AQ** to be about 0.1–0.2 eV, which is well reproduced with the lower ω value. In addition, we find that experimental oscillator strength for absorption (f_{abs} = 0.19) is accurately reproduced with ω = 0.040 whereas about twice this value is obtained with ω = 0.100. Note, that the same trend of increasing oscillator strength with the amount of HFX is also seen in Fig. 6.

Independently of the value of ω, we find two crucial differences between **Cz-BDT** and **Cz-AQ**, which explain its lower TADF

26146 | *Phys. Chem. Chem. Phys.*, 2021, **23**, 26135–26150

This journal is © the Owner Societies 2021

Table 5 Summary of the photophysical data for the four molecules studied

	$E_{abs,max}$ (eV)	f_{abs}	$E_{em,max}$ (eV)	f_{em}	Φ	$\Delta E_{ST,vert.}$ (eV)	$\Delta E_{ST,ad.}$ (eV)
Cz-BDT ($\omega = 0.040$)	1.94	0.181	1.71	0.000	—	0.19	0.36
Cz-BDT ($\omega = 0.100$)	2.71	0.478	2.06	0.000	—	0.54	0.58
Cz-BDT (exp.)[a]	2.65	—	1.87	—	0.095	—	—
Cz-AQ ($\omega = 0.040$)	2.14	0.184	1.86	0.106	—	0.02	0.11
Cz-AQ ($\omega = 0.100$)	2.97	0.453	2.49	0.340	—	0.35	0.49
Cz-AQ (exp.)[b]	2.91	0.19	2.22	—	0.60	—	0.1–0.2[c]
Cz-BDT-SO$_2$ ($\omega = 0.040$)	1.21	0.553	0.44	0.000	—	0.29	0.04
Cz-BDT-SO$_2$ ($\omega = 0.100$)	1.73	0.684	1.41	0.511	—	0.51	0.63
Cz-BDF ($\omega = 0.040$)	1.95	0.151	1.69	0.000	—	0.28	0.43
Cz-BDF ($\omega = 0.100$)	2.73	0.419	1.99	0.000	—	0.60	0.63

[a] Ref. 34, measured in toluene. [b] Ref. 4, measured in toluene. [c] Estimated from data in ref. 4.

efficiency. First, the larger singlet–triplet gap of **Cz-BDT** (considering vertical and adiabatic values) will hamper repopulation of S$_1$. Second, the vanishing oscillator strength for emission (f_{em}) of **Cz-BDT** will slow down emission from S$_1$ even if it is populated. Conversely, **Cz-AQ** obtains a strongly emissive S$_1$ state due to symmetry breaking.

Considering all four molecules studied, the absorption energies are arranged as **Cz-AQ** > **Cz-BDF** ≈ **Cz-BDT** ≫ **Cz-BDT-SO$_2$** reflecting the different acceptor properties of the cores used. **Cz-BDF** is not expected to be a suitable TADF chromophore due to its similar properties to **Cz-BDT**, i.e. large singlet–triplet gap and vanishing oscillator strength for emission. The conclusion is not so clear for **Cz-BDT-SO$_2$** due to the strong discrepancy between the results using the two ω values.

Reviewing Fig. 10, we can speculate that, aside from its lower singlet–triplet gap, **Cz-AQ** also profits from a high density of states connecting the T$_1$ and S$_1$ states (see also ref. 11). In addition, the presence of nπ^* states in this area is expected to mediate SOC efficiently. The presence of a number of different excited states with varying properties, as found here, is certainly consistent with the rich photophysics measured experimentally for a related D–**AQ**–D molecules.[94,95]

4.2 Differences between singlet and triplet states

A striking observation made in the above plots relates to the differences in excited state character found between singlet and triplet states. It is tempting to think of singlet and triplet excited states as involving the same orbital transitions, only differing in their spin coupling. However, the above results show that this picture is oversimplified for realistic push–pull systems. Specifically, we find that low energy triplet states have enhanced local character whereas CT is enhanced for the singlets. This is reflected in all the bar graphs shown in the centre panels of Fig. 9–11 with enhanced blue and orange bars for the triplets and more red/green for the singlets. The difference is even more apparent in terms of the exciton sizes (bottom panels of Fig. 9–11) showing that the triplet states (red dots) are consistently below the singlet states (black dots).

Differences between singlet and triplet states can be understood by considering the different contributing energy terms.[1,5,7,33] Singlet and triplet states are both affected by an attractive Coulomb interaction favouring locally excited states while singlets are also affected by a repulsive exchange interaction

favouring CT states.[5] The effect on exchange for triplet energies is a bit more ambiguous and depends on the reference chosen. If one considers the Kohn–Sham orbital energies as reference, then one finds that triplets are independent of any exchange contribution.[5] However, if one further considers that the LUMO energy is lowered by the exchange interaction between HOMO and LUMO, then one finds that triplet energies are indeed stabilised by this exchange interaction.[7] Independently of this discussion one finds that low-energy triplets should be more localised, which is well represented by the data shown. Furthermore, the above plots highlight the differences between singlet and triplet states, which cannot be explained by simply reordering the states without also mixing them. Clearly, there is no one-to-one correspondence between the singlet and triplet states.

These differences are important for at least three reasons. First, it should be understood that the photophysics of these molecules cannot be understood in terms of a simplified picture containing only two or three MOs but that a number of terms ultimately influence the final energies of the states. In this context, it has been pointed out, before, that the idealised picture where singlets and triplets differ by twice the exchange energy would only hold if their wavefunctions were the same except for the spin coupling.[96] Discussions of how to go beyond this and understand singlet–triplet gaps within and beyond the orbital picture are provided in ref. 5 and 33. Second, the discussion shows that the available space for molecular design is larger than one would anticipate viewing only two or three MOs. Indeed, there are a large number of terms that can potentially be fine-tuned to optimise the overall photophysics. Third, differences in the wavefunctions of singlet and triplet states explain why singlets and triplets differ strongly in their computational description using, e.g., TDDFT[69,97] or the Bethe–Salpeter equation.[98] Being aware of these differences may help in the development of computational methods that provide a balanced and accurate description of singlets and triplets.

4.3 Methodological aspects

Reviewing the computations within this manuscript we found that the density functional used, and in particular the amount of non-local HFX, plays a critical role. As shown in Fig. 6 and Table 5 increasing the amount of HFX has four critical consequences: (i) raising the overall excitation energies, (ii) widening ΔE_{ST}, (iii) reducing CT character, and (iv) increasing oscillator strengths. This illustrates how a change in density functional

This journal is © the Owner Societies 2021

Phys. Chem. Chem. Phys., 2021, **23**, 26135–26150 | **26147**

does not only shift excitation energies but potentially affects many different aspects of the predicted photophysics. Table 5 highlights the challenges in finding a method that describes all aspects correctly: using an ω value of 0.100 improves absorption and emission energies whereas a value of 0.040 gives better singlet triplet gaps and oscillator strengths.

Furthermore, we found that geometry optimisation in the excited state was critical for two individual effects. First, it allowed for adjustments in the torsion angles altering delocalisation and CT for the individual states. Second, it was seen as the basis for excited state symmetry breaking yielding a strongly emissive state for **Cz-AQ** whereas for **Cz-BDT** the S_1 state remained dark at its symmetric minimum.

Solvation effects were considered using three different approaches: the LR-PCM and SS-PCM methods in connection with TDDFT as well as ground-state PCM in connection with UKS. It was found that the different solvation models produced different excitation energies, especially in terms of a stabilisation of CT states. However, differences between these solvation models were comparatively small suggesting that the choice of solvation model is not as critical as the choice of density functional and an appropriate treatment of geometry relaxation, at least for weakly polar solvents.

5 Conclusions

Within this work, we have presented a detailed study of four closely related D–π–A–π–D molecules: the effective TADF chromophore **Cz-AQ**, its close analogue **Cz-BDT**, which undergoes red-shifted TADF albeit with a much lower quantum yield, and two molecules not yet synthesised **Cz-BDT-SO$_2$** and **Cz-BDF**. After presenting the main structural parameters, we have presented a detailed evaluation of computational methods benchmarking five density functionals to experimental absorption data and the high-level *ab initio* computational reference ri-ADC(2). This highlighted that not only the energies but also the overall wavefunctions depend heavily on the functional used and particularly the amount of Hartree–Fock exchange. Increased HFX was found to raise the computed absorption and emission energies, singlet–triplet gaps, and oscillator strengths; we have highlighted the challenges of producing accurate results for all four values simultaneously.

Using the ωPBEh functional, which was shown to represent energies and wavefunctions accurately, we have studied excited-state minima in solution. The **Cz-AQ** and **Cz-BDT** molecules were shown to not only differ in terms of their singlet–triplet gaps but we also highlighted the importance of planarisation and excited-state symmetry breaking leading to markedly different photophysics between the molecules despite their similar molecular structures. In addition, we have related the strong TADF activity of **Cz-AQ** to the existence of a strongly emissive symmetry broken S_1 minimum with CT character whereas **Cz-BDT** formed a dark locally excited S_1 minimum. Moreover, **Cz-AQ** was characterised by a dense set of states of different character connecting the T_1 and S_1 states providing a pathway between them.

In a more general sense, we showed that a detailed analysis of excited-state wavefunctions can provide insight into the photophysics of push–pull systems far beyond a simple analysis of energies and frontier orbitals. General differences between singlet and triplet states have been outlined with triplets being more compact and local whereas enhanced CT was found for singlets. We believe that the presented protocol will be valuable for studying various push–pull systems in the future providing detailed insight into the properties of existing chromophores and providing new design ideas for the future.

Conflicts of interest

There are no conflicts to declare.

Acknowledgements

References

1 F. B. Dias, T. J. Penfold and A. P. Monkman, *Methods Appl. Fluoresc.*, 2017, **5**, 012001.

2 Z. Yang, Z. Mao, Z. Xie, Y. Zhang, S. Liu, J. Zhao, J. Xu, Z. Chi and M. P. Aldred, *Chem. Soc. Rev.*, 2017, **46**, 915–1016.

3 M. Godumala, S. Choi, M. J. Cho and D. H. Choi, *J. Mater. Chem. C*, 2019, **7**, 2172–2198.

4 Q. Zhang, H. Kuwabara, W. J. Potscavage, S. Huang, Y. Hatae, T. Shibata and C. Adachi, *J. Am. Chem. Soc.*, 2014, **136**, 18070–18081.

5 P. Kimber and F. Plasser, *Phys. Chem. Chem. Phys.*, 2020, **22**, 6058–6080.

6 P. K. Samanta, D. Kim, V. Coropceanu and J.-L. Brédas, *J. Am. Chem. Soc.*, 2017, **139**, 4042–4051.

7 X. K. Chen, D. Kim and J. L. Brédas, *Acc. Chem. Res.*, 2018, **51**, 2215–2224.

8 J. M. Mewes, *Phys. Chem. Chem. Phys.*, 2018, **20**, 12454–12469.

9 J. Gibson, A. P. Monkman and T. J. Penfold, *ChemPhysChem*, 2016, **17**, 2956–2961.

10 A. Y. Freidzon and A. A. Bagaturyants, *J. Phys. Chem. A*, 2020, **124**, 7927–7934.

11 J. Eng, J. Hagon and T. J. Penfold, *J. Mater. Chem. C*, 2019, **7**, 12942–12952.

12 B. Dereka, D. Svechkarev, A. Rosspeintner, A. Aster, M. Lunzer, R. Liska, A. M. Mohs and E. Vauthey, *Nat. Commun.*, 2020, **11**, 1–11.

13 A. Dreuw, J. L. Weisman and M. Head-Gordon, *J. Chem. Phys.*, 2003, **119**, 2943–2946.

14 S. A. Mewes, F. Plasser, A. Krylov and A. Dreuw, *J. Chem. Theory Comput.*, 2018, **14**, 710–725.

26148 | *Phys. Chem. Chem. Phys.*, 2021, **23**, 26135–26150

This journal is © the Owner Societies 2021

15 S. Huang, Q. Zhang, Y. Shiota, T. Nakagawa, K. Kuwabara, K. Yoshizawa and C. Adachi, *J. Chem. Theory Comput.*, 2013, **9**, 3872–3877.

16 J. Shee and M. Head-Gordon, *J. Chem. Theory Comput.*, 2020, **16**, 6244–6255.

17 L. Kunze, A. Hansen, S. Grimme and J.-M. Mewes, *J. Phys. Chem. Lett.*, 2021, **12**, 8470–8480.

18 R. Improta, V. Barone, G. Scalmani and M. J. Frisch, *J. Chem. Phys.*, 2006, **125**, 054103.

19 J. M. Mewes, Z. Q. You, M. Wormit, T. Kriesche, J. M. Herbert and A. Dreuw, *J. Phys. Chem. A*, 2015, **119**, 5446–5464.

20 Y. Olivier, B. Yurash, L. Muccioli, G. D'Avino, O. Mikhnenko, J. C. Sancho-García, C. Adachi, T.-Q. Nguyen and D. Beljonne, *Phys. Rev. Mater.*, 2017, **1**, 075602.

21 T. J. Penfold, F. B. Dias and A. P. Monkman, *Chem. Commun.*, 2018, **54**, 3926–3935.

22 A. V. Luzanov, A. A. Sukhorukov and V. E. Umanskii, *Theor. Exp. Chem.*, 1976, **10**, 354–361.

23 M. J. G. Peach, P. Benfield, T. Helgaker and D. J. Tozer, *J. Chem. Phys.*, 2008, **128**, 044118.

24 C. A. Guido, P. Cortona and C. Adamo, *J. Chem. Phys.*, 2014, **140**, 104101.

25 T. Etienne, X. Assfeld and A. Monari, *J. Chem. Theory Comput.*, 2014, **10**, 3896–3905.

26 P. Petelenz and B. Pac, *J. Am. Chem. Soc.*, 2013, **135**, 17379–17386.

27 F. Plasser, B. Thomitzni, S. A. Bäppler, J. Wenzel, D. R. Rehn, M. Wormit and A. Dreuw, *J. Comput. Chem.*, 2015, **36**, 1609–1620.

28 S. A. Bäppler, F. Plasser, M. Wormit and A. Dreuw, *Phys. Rev. A: At., Mol., Opt. Phys.*, 2014, **90**, 052521.

29 S. A. Mewes, F. Plasser and A. Dreuw, *J. Phys. Chem. Lett.*, 2017, **8**, 1205–1210.

30 S. Mai, F. Plasser, J. Dorn, M. Fumanal, C. Daniel and L. González, *Coord. Chem. Rev.*, 2018, **361**, 74–97.

31 F. Glöcklhofer, A. Rosspeintner, P. Pasitsuparoad, S. Eder, J. Fröhlich, G. Angulo, E. Vauthey and F. Plasser, *Mol. Syst. Des. Eng.*, 2019, **4**, 951–961.

32 Z. Pei, J. Yang, J. Deng, Y. Mao, Q. Wu, Z. Yang, B. Wang, C. M. Aikens, W. Liang and Y. Shao, *Phys. Chem. Chem. Phys.*, 2020, **22**, 26852–26864.

33 Z. Pei, Q. Ou, Y. Mao, J. Yang, A. de la Lande, F. Plasser, W. Liang, Z. Shuai and Y. Shao, *J. Phys. Chem. Lett.*, 2021, **12**, 2712–2720.

34 S. Montanaro, A. J. Gillett, S. Feldmann, E. W. Evans, F. Plasser, R. H. Friend and I. A. Wright, *Phys. Chem. Chem. Phys.*, 2019, **21**, 10580–10586.

35 L. Ye, S. Zhang, W. Zhao, H. Yao and J. Hou, *Chem. Mater.*, 2014, **26**, 3603–3605.

36 L. Ye, X. Jiao, H. Zhang, S. Li, H. Yao, H. Ade and J. Hou, *Macromolecules*, 2015, **48**, 7156–7163.

37 D. Patra, W. Budiawan, T. Y. Huang, K. H. Wei, P. C. Wang, K. C. Ho, M. Al-Hashimi and C. W. Chu, *ACS Appl. Energy Mater.*, 2018, **1**, 3684–3692.

38 G. Huang, H. Jiang, J. Zhang, F. Liu, M. Zhu, H. Tan, Y. Wang, W. Chen, R. Yang and W. Zhu, *ACS Appl. Energy Mater.*, 2018, **1**, 1506–1511.

39 T. Nakamura, *Macromolecules*, 2020, **53**, 9836–9846.

40 T. J. Aldrich, W. Zhu, S. Mukherjee, L. J. Richter, E. Gann, D. M. DeLongchamp, A. Facchetti, F. S. Melkonyan and T. J. Marks, *Chem. Mater.*, 2019, **31**, 4313–4321.

41 T. J. Aldrich, A. S. Dudnik, N. D. Eastham, E. F. Manley, L. X. Chen, R. P. Chang, F. S. Melkonyan, A. Facchetti and T. J. Marks, *Macromolecules*, 2018, **51**, 9140–9155.

42 K. Kobayashi, C. L. Gajurel, K. Umemoto and Y. Mazaki, *Bull. Chem. Soc. Jpn.*, 1992, **65**, 2168–2172.

43 S. Yamaguchi, H. Tatemitsu, Y. Sakata and S. Misumi, *Chem. Lett.*, 1983, 1229–1230.

44 J. H. Kim, J. H. Yun and J. Y. Lee, *Adv. Opt. Mater.*, 2018, **6**, 1800255.

45 C. J. Christopherson, D. M. Mayder, J. Poisson, N. R. Paisley, C. M. Tonge and Z. M. Hudson, *ACS Appl. Mater. Interfaces*, 2020, **12**, 20000–20011.

46 D. G. Congrave, B. H. Drummond, P. J. Conaghan, H. Francis, S. T. Jones, C. P. Grey, N. C. Greenham, D. Credgington and H. Bronstein, *J. Am. Chem. Soc.*, 2019, **141**, 18390–18394.

47 J. Chen, W. Tao, W. Chen, Y. Xiao, K. Wang, C. Cao, J. Yu, S. Li, F. Geng, C. Adachi, C. Lee and X. Zhang, *Angew. Chem., Int. Ed.*, 2019, **58**, 14660–14665.

48 X. Gong, P. Li, Y. Huang, C. Wang, C. Lu, W. Lee, C. Zhong, Z. Chen, W. Ning, C. Wu, S. Gong and C. Yang, *Adv. Funct. Mater.*, 2020, **30**, 1908839.

49 E. Avellanal-Zaballa, A. Prieto-Castaneda, F. Garcia-Garrido, A. R. Agarrabeitia, E. Rebollar, J. Banuelos, I. Garcia-Moreno and M. J. Ortiz, *Chem. – Eur. J.*, 2020, **26**, 16080–16088.

50 T. Yang, Z. Cheng, Z. Li, J. Liang, Y. Xu, C. Li and Y. Wang, *Adv. Funct. Mater.*, 2020, **30**, 2002681.

51 B. Zhao, H. Wang, C. Han, P. Ma, Z. Li, P. Chang and H. Xu, *Angew. Chem., Int. Ed.*, 2020, **59**, 19042–19047.

52 P. Kautny, F. Glöcklhofer, T. Kader, J.-M. Mewes, B. Stöger, J. Fröhlich, D. Lumpi and F. Plasser, *Phys. Chem. Chem. Phys.*, 2017, **19**, 18055–18067.

53 S. Zhen, S. Wang, S. Li, W. Luo, M. Gao, L. G. Ng, C. C. Goh, A. Qin, Z. Zhao, B. Liu and B. Z. Tang, *Adv. Funct. Mater.*, 2018, **28**, 1706945.

54 E. Varathan and V. Subramanian, *Phys. Chem. Chem. Phys.*, 2017, **19**, 12002–12012.

55 E. Varathan and A. Patnaik, *J. Phys. Chem. A*, 2019, **123**, 8755–8765.

56 F. Plasser, *J. Chem. Phys.*, 2020, **152**, 084108.

57 F. Plasser, M. Wormit and A. Dreuw, *J. Chem. Phys.*, 2014, **141**, 024106.

58 F. Plasser and H. Lischka, *J. Chem. Theory Comput.*, 2012, **8**, 2777–2789.

59 R. L. Martin, *J. Chem. Phys.*, 2003, **118**, 4775–4777.

60 F. Plasser, A. J. Aquino, W. L. Hase and H. Lischka, *J. Phys. Chem. A*, 2012, **116**, 11151–11160.

61 S. Rupp, F. Plasser and V. Krewald, *Eur. J. Inorg. Chem.*, 2020, 1506–1518.

62 P. A. Sánchez-Murcia, J. J. Nogueira, F. Plasser and L. González, *Chem. Sci.*, 2020, **11**, 7685–7693.

63 S. Yang, D. Streater, C. Fiankor, J. Zhang and J. Huang, *J. Am. Chem. Soc.*, 2021, **143**, 1061–1068.

This journal is © the Owner Societies 2021

Phys. Chem. Chem. Phys., 2021, **23**, 26135–26150 | **26149**

64 N. Mardirossian and M. Head-Gordon, *Phys. Chem. Chem. Phys.*, 2014, **16**, 9904–9924.

65 F. Weigend and R. Ahlrichs, *Phys. Chem. Chem. Phys.*, 2005, **7**, 3297–3305.

66 C. Hättig, *Adv. Quantum Chem.*, 2005, **50**, 37–60.

67 A. Schäfer, C. Huber and R. Ahlrichs, *J. Chem. Phys.*, 1994, **100**, 5829–5835.

68 S. Hirata and M. Head-Gordon, *Chem. Phys. Lett.*, 1999, **314**, 291–299.

69 M. J. Peach, M. J. Williamson and D. J. Tozer, *J. Chem. Theory Comput.*, 2011, **7**, 3578–3585.

70 J. P. Perdew, K. Burke and M. Ernzerhof, *Phys. Rev. Lett.*, 1996, **77**, 3865–3868.

71 C. Adamo and V. Barone, *J. Chem. Phys.*, 1999, **110**, 6158–6170.

72 M. A. Rohrdanz, K. M. Martins and J. M. Herbert, *J. Chem. Phys.*, 2009, **130**, 054112.

73 T. Yanai, D. P. Tew and N. C. Handy, *Chem. Phys. Lett.*, 2004, **393**, 51–57.

74 A. D. Becke, *J. Chem. Phys.*, 1993, **98**, 5648–5652.

75 C. Lee, W. Yang and R. G. Parr, *Phys. Rev. B: Condens. Matter Mater. Phys.*, 1988, **37**, 785–789.

76 V. Barone and M. Cossi, *J. Phys. Chem. A*, 1998, **102**, 1995–2001.

77 M. Cossi, N. Rega, G. Scalmani and V. Barone, *J. Comput. Chem.*, 2003, **24**, 669–681.

78 R. Cammi and B. Mennucci, *J. Chem. Phys.*, 1999, **110**, 9877–9886.

79 M. Cossi and V. Barone, *J. Chem. Phys.*, 2001, **115**, 4708–4717.

80 Z. Q. You, J. M. Mewes, A. Dreuw and J. M. Herbert, *J. Chem. Phys.*, 2015, **143**, 204104.

81 J. M. Mewes, J. M. Herbert and A. Dreuw, *Phys. Chem. Chem. Phys.*, 2017, **19**, 1644–1654.

82 E. Epifanovsky, *et al.*, *J. Chem. Phys.*, 2021, **155**, 084801.

83 Turbomole V7.2 2017, a development of University of Karlsruhe and Forschungszentrum Karlsruhe GmbH, 1989–2007, TURBOMOLE GmbH, since 2007, available from http://www.turbomole.com.

84 Supporting research data available: molecular geometries, input/output files of Q-Chem and Turbomole, DOI: 10.17028/rd.lboro.15111870.

85 D. Kánnár and P. G. Szalay, *J. Mol. Model.*, 2014, **20**, 2503.

86 B. Kozma, A. Tajti, B. Demoulin, R. Izsák, M. Nooijen and P. G. Szalay, *J. Chem. Theory Comput.*, 2020, **16**, 4213–4225.

87 D. J. Tozer, R. D. Amos, N. C. Handy, B. O. Roos and L. Serrano-Andres, *Mol. Phys.*, 1999, **97**, 859–868.

88 S. A. Mewes, F. Plasser and A. Dreuw, *J. Chem. Phys.*, 2015, **143**, 171101.

89 S. Bai, R. Mansour, L. Stojanović, J. M. Toldo and M. Barbatti, *J. Mol. Model.*, 2020, **26**, 1–9.

90 R. Baer, E. Livshits and U. Salzner, *Annu. Rev. Phys. Chem.*, 2010, **61**, 85–109.

91 L. Kronik, T. Stein, S. Refaely-Abramson and R. Baer, *J. Chem. Theory Comput.*, 2012, **8**, 1515–1531.

92 G. M. Barca, A. T. Gilbert and P. M. Gill, *J. Chem. Theory Comput.*, 2018, **14**, 1501–1509.

93 Z. Szakács, F. Glöcklhofer, F. Plasser and E. Vauthey, *Phys. Chem. Chem. Phys.*, 2021, **23**, 15150–15158.

94 J. Choi, D.-S. Ahn, K. Y. Oang, D. W. Cho and H. Ihee, *J. Phys. Chem. C*, 2017, **121**, 24317–24323.

95 Z. Kuang, G. He, H. Song, X. Wang, Z. Hu, H. Sun, Y. Wan, Q. Guo and A. Xia, *J. Phys. Chem. C*, 2018, **122**, 3727–3737.

96 D. Kim, *J. Phys. Chem. C*, 2015, **119**, 12690–12697.

97 D. Jacquemin, E. A. Perpète, I. Ciofini and C. Adamo, *J. Chem. Theory Comput.*, 2010, **6**, 1532–1537.

98 D. Jacquemin, I. Duchemin, A. Blondel and X. Blase, *J. Chem. Theory Comput.*, 2017, **13**, 767–783.

26150 | *Phys. Chem. Chem. Phys.*, 2021, **23**, 26135–26150

This journal is © the Owner Societies 2021